

mmFall: Fall Detection using 4D MmWave Radar and Variational Recurrent Autoencoder

Feng Jin, *Student Member, IEEE*, Arindam Sengupta, *Student Member, IEEE*, and Siyang Cao, *Member, IEEE*

Abstract—Elderly fall prevention and detection is extremely crucial especially with the fast aging society. In this paper, we propose *mmFall*, a novel system for fall detection. In terms of sensing modality, we adopt the emerging millimeter-wave (mmWave) radar sensor to collect the point cloud of a moving human body along with its estimated centroid. In terms of detection methodology, we propose a variational recurrent autoencoder (VRAE) model to monitor the motion anomaly level, and claim a fall detection when two conditions meet simultaneously, viz. (i) a anomaly level spike and (ii) a sudden drop of body’s centroid height. The mmWave radar sensor provides advantages, such as privacy-compliance and high sensitivity to motion, over the traditional sensing modalities. To overcome the difficulties in machine learning using radar due to the data randomness, the VRAE uses variational inference, a probabilistic approach rather than deterministic approach, to infer the posterior probability of latent motion state at every frame, followed by a recurrent neural network (RNN) to learn the temporal features of the motion over multiple frames. Moreover, to circumvent the difficulties in fall data collection and labeling in the traditional fall detection research, the VRAE is built upon an autoencoder architecture, a semi-supervised approach, and trained with only normal activities of daily living (ADL) such that in the inference stage the VRAE will generate a spike in the anomaly level once an abnormal motion, such as fall, occurs. During the experiment¹, we implemented the VRAE along with two other baselines, and tested on the dataset collected in an apartment. The receiver operating characteristic (ROC) curve indicates that our proposed model outperforms the other two baselines, and achieves 98% detection out of 50 falls at expense of just 2 false alarms.

Index Terms—Fall detection, millimeter wave radar, variational autoencoder, recurrent autoencoder, semi-supervised learning, anomaly detection.

I. INTRODUCTION

GLOBALLY, the elderly aged 65 or over make up the fastest-growing age group. In fact, the proportion of the elderly in the world is projected to reach nearly 12% by 2030 from 9% in 2019 [1]. Approximately 28-35% of the elderly fall every year [2], and suffer the greatest number of fatal falls, making it the second leading cause of unintentional injury death after road traffic injuries [3].

Copyright (c) 2015 IEEE. Personal use of this material is permitted. However, permission to use this material for any other purposes must be obtained from the IEEE by sending a request to pubs-permissions@ieee.org.

Feng Jin, Arindam Sengupta and Siyang Cao are with Department of Electrical and Computer Engineering, *the University of Arizona*, Tucson, AZ, 85719 USA. (e-mail: {fengjin, sengupta, caos}@email.arizona.edu)

¹All the codes and dataset are shared on Github (<https://github.com/radar-lab/mmfall>).

Moreover, elderly falls are extremely expensive. Only in the United States in 2015, the total direct cost of fall among the elderly, adjusted for inflation, was 31.9 billion USD [4]. As a result, measures to protect the elderly from fall injuries becomes increasingly urgent from both a social and economic perspective.

Physical training program, such as Simplified Tai Chi, can assist in reducing fall risks [5], while it is beyond the research scope of information technology (IT). In the IT community, researchers seek to (i) either predict the fall right before it occurs so that a mechanism, such as a wearable airbag [6] or a walking-aid cane robot [7], can be deployed to reduce the fall injuries; or (ii) detect the fall right after it occurs along with an alert sent to the caregiver immediately so a timely treatment can be implemented [8]. Based on the type of sensor to capture data for body motion analysis, the fall-related research can be divided into three categories, i.e. wearable, non-wearable and fusion solutions [8].

Wearable solutions normally require the elderly to carry single or several sensors on their body. These sensors can measure the motion parameters, such as acceleration (accelerometer), angular velocity (gyroscope), orientation (magnetometer), and tilt angle (inclinometer), among others. Thus, a fall can be predicted or detected by analyzing the sudden change of body motion or posture [9]–[11]. On the other hand, non-wearable solutions place sensors in the environment to monitor the elderly motion. One of the primary non-wearable sensors is camera, that provides rich motion details visually such that the silhouette change can be perceived over time in order to predict or detect the fall [12]. Some ambient sensors, which provide acoustic [13], vibration [14], thermal [15], radio frequency (RF) [16] changes in the environment when a fall occurs, have also be used in the past. Furthermore, depth sensors, which generate the depth information per pixel, have also been used to track the joint motion to detect fall [17]. Radar sensors have also been used to capture the distinguish micro-Doppler pattern for fall detection [18]. Beside wearable and non-wearable solutions, the fusion solution involves multiple heterogeneous sensors, which can potentially improve the reliability and specificity of fall-related systems [19].

In this paper, we are focusing on non-wearable fall detection using the emerging millimeter-wave (mmWave) radar sensor [20]. In short, mmWave radar sensor measures the point cloud coming from moving objects in a scene. Each point in the radar point cloud contains a 3D position

and a 1-D Doppler (radial velocity component) information, thereby resulting in a 4D mmWave radar as referred to in the paper title. In the fall detection application, mmWave radar sensor can offer several advantages over the other traditional sensing technologies, viz. (i) non-intrusive and convenient over the wearable solutions that require the elderly cooperation and compliance to be worn, and also need frequent battery recharging; (ii) privacy-compliant over camera, as video monitoring violates the privacy of the elderly daily life; (iii) sensitive to motion and operationally robust to occlusions compared to depth sensor, especially in a complex living environment; (iv) more informative over typical ambient sensors which suffer interference from the external environment [21]; and (v) low-cost, compact and high resolution over the traditional radars.

Now, we restrict our attention to radar-related fall detection research for detection methodology review. Traditionally, radar-related fall detection system collects fall data, applies time-frequency analysis to extract the micro-Doppler features [22], and then detects the fall with a classifier, as fall has a unique micro-Doppler signature than other motions. In [23], the authors pre-screened simulated falls from stunt actors collected by a Doppler radar, proposed to use Wavelet transform (WT) to extract the features and estimated the wavelet coefficients from the simulated falls, and then detected fall using the nearest neighbor (NN) approach based on the feature distance between real-life motion sample and the simulated fall samples. In [24], the authors used a range-Doppler radar to capture the spectrogram of human motion as a micro-Doppler signature, and gathered the range map at the same time in order to distinguish fall from sitting/bending, by training a logistic regression model with labeled data on simulated falls and non-falls.

However, these traditional approaches have several major drawbacks. First, the problem in these supervised approaches, that need manually preprocessed fall data samples for feature extraction and classifier training, is that the fall is very difficult to collect as the fall event is rare and non-continuous, not to mention the impossible ask of the elderly repeating falls for data collection. Moreover, the simulated fall from stunt actor may differ from the real-life elderly fall. Meanwhile, the fall data labeling procedure is very expensive as it requires manual extraction of short portions of fall event from a long duration recordings. Secondly, no target separation is considered in these traditional approaches. This may cause problems when there are interfering sources in motion, for example ceiling fans, as in this case the most commonly used time-frequency extractor would take in a mix of motion from target human body and interference.

To overcome these drawbacks, we use mmWave radar sensor which clusters and tracks multiple moving targets in a scene so that interference can be excluded from the target human's body, and leverage the semi-supervised anomaly detection approach to circumvent difficulties in the real-life elderly fall collection. Anomaly detection refers to the problem of finding patterns in data that do not conform to

expected behavior [25]. In our case, the expected behaviors would be the normal activities of daily living (ADL), such as walking/sitting/crouching and etc., while a fall does not conform to these normal behaviors. The semi-supervised anomaly detection method, for example autoencoder, trains a model with only normal ADL without data labeling. Thus, the model will 'recognize' these normal ADL, while a fall will 'surprise' the model.

Particularly, we propose a variational recurrent autoencoder (VRAE) to learn the radar point cloud in a probabilistic way rather than deterministic way on account of the radar data randomness. In the encoding part, VRAE learns the posterior probability of the target human body's latent motion state at each frame through variational inference, following a recurrent neural network for temporal feature compression over multiple frames. In the decoding part, the VRAE tries to reconstruct the likelihood of the input radar data, given a latent motion state sequence recovered from the encoding part. This model will be trained only with normal ADL data, and output low loss, also denoted as anomaly level, during normal ADL occurrence. Then we claim a fall detection when there is a spike in the anomaly level and a sudden drop of the body's centroid height, which is also monitored by the radar sensor in parallel, at the same time.

This rest of this paper is organized as follows. Section II introduces all the components that constitutes our proposed *mmFall* system, including the principles of mmWave radar sensor, variational inference, variational autoencoder, and recurrent autoencoder. Section III presents the details of proposed *mmFall* system, including the overall system architecture, a novel data oversampling method and a custom loss function for model training. Section IV shows the experimental results conducted in an apartment, and compares the performance of our model with two baselines. Finally, section V concludes the paper.

II. PRELIMINARIES

In this section, we introduce the background of all the components that constitute the proposed *mmFall* system detailed in the next section.

A. 4D mmWave FMCW Radar Sensor

The carrier frequency of mmWave frequency-modulated continuous wave (FMCW) radar sensor, or mmWave radar sensor for short, ranges from 57 GHz to 85 GHz according to various applications. For example, 76-81 GHz is primarily used for automotive application such as objects' dynamics measurement [26], and 57-64 GHz can be used for short-range interactive motion sensing such as in the Google's Soli project [27]. Coming along with the high carrier frequency, a high bandwidth up to 4 GHz is available, and the physical size of hardware components including antennas shrinks. This eventually makes the mmWave radar sensor more compact and higher resolution than the traditional low-frequency band radars.

There are no big differences in signal modulation and processing of mmWave radar sensor than that of conventional FMCW radars described in [28]. Generally, the mmWave radar sensor transmits multiple linear FMCW signals over multiple antenna channels in both azimuth and elevation. After the stretch processing and digitalization, a raw multidimensional radar data cube is obtained. Followed by a series of fast Fourier transform (FFT), the parameters of each reflection point in a scene, i.e. range r , azimuth angle θ_{AZ} , elevation angle θ_{EL} , and Doppler D , are estimated. In addition, during this process the constant false alarm rate (CFAR) is incorporated to detect the points above a given signal-to-noise ratio (SNR) against the surrounding noise, and the moving target indication (MTI) is applied to distinguish the moving points from the static background. Eventually, a set of moving points, also called radar point cloud, is obtained.

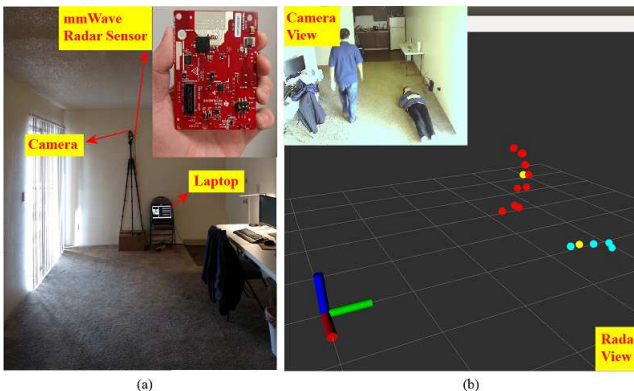


Fig. 1: MmWave radar sensor and radar point cloud. (a) The mmWave radar sensor is setup in an apartment, the camera provides a view for reference, and the laptop is used for data acquisition. The same setup is also used in the experiment in Section IV. (b) Radar point cloud in a two-person scenario. One is laying down on the floor and the other one is walking. For the points, different color indicates different person while the yellow point indicates the centroid. For the coordinates, red is the cross-radar direction, green is the forward direction, and blue is the height direction. The original radar measurement of each point is a vector of $(r, \theta_{AZ}, \theta_{EL}, D)$, along with the estimated centroid of (x_c, y_c, z_c) .

If multiple moving targets are present in a scene, the obtained point cloud is a collection of such points from all targets. Thus, a clustering method, for example the density-based spatial clustering of applications with noise (DBSCAN), has to be applied to group a subset of points into single target such that multiple targets can be separated. Meanwhile, the centroid of target can be estimated from the point subset associated with it. Followed by a tracking algorithm, such as Kalman filtering, the trajectory of each target will be recorded with a association of an unique target ID. Particularly, a joint clustering/tracking algorithm call Group Tracking [29] can be used as well. Fig. 1 shows the mmWave radar sensor and the radar point cloud we can get from it. With the target ID, the motion history of each target can be gathered separately in a multiple-target scenario, such that we are able to analyze each target's motion individually.

For simplicity but without loss of generality, we will discuss single-person scenario thereafter.

B. Radar Point Cloud Distribution for Human Body Motion

From the Fig. 1 (b), a straightforward fall detection approach is to analyze the height of the body centroid. For instance, if the body centroid suddenly drops to the ground level, then a fall event is detected. However, this approach may easily cause a false alarm when crouching or sitting.

Considering the randomness of radar measurement, now we start to view the radar point cloud of human body as a probabilistic distribution. From the observation of Fig. 1 (b), we make an assumption as

Assumption 1. At each frame, the radar point cloud of human body, denoted as \mathbf{X} , follows a specific multivariate Gaussian distribution whose mean is relevant to the body centroid and covariance is relevant to the body shape. The body motion state, such as walking/fall, is a latent variable denoted as \mathbf{z} . Given a \mathbf{z} , the change of distribution \mathbf{X} over multiple frames has an unique pattern, which is named as motion pattern.

For example, the radar point cloud of a laying-down (on the floor) person may have large variance in x/y -axis but small variance in z -axis, while the radar point cloud of a walking person may have small variance in x/y -axis but large variance in z -axis. A depiction of such motion pattern is shown in Fig. 2.

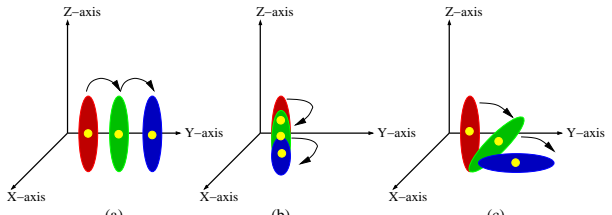


Fig. 2: A depiction of motion pattern, i.e. the radar point cloud distribution change over multiple frames, for different motions. The ellipse represents the distribution, and the yellow point indicates the centroid. Different color indicates the frame in time order: red, green, and then blue. (a) Walking; (b) Crouching; (c) Fall.

Although the Assumption 1 might not be true as we never know the true physical generation process of radar data from a human body, we at least believe that this assumption is enough for our purpose, i.e. distinguish different motion of human body. Therefore, intuitively we propose to detect fall through ‘learning’ the uniqueness of such motion pattern.

The overview of following subsections is that, we propose to (i) learn the distribution at each frame through variational inference, (ii) learn the distribution change over multiple frames through recurrent neural network, (iii) and overall they are discussed in the framework of autoencoder for semi-supervised learning approach.

C. Variational Inference

More formally, at each frame we obtain a N -point radar point cloud $\mathbf{X} = \{\mathbf{x}_n\}_{n=1}^N$. The original radar mea-

surement of each point \mathbf{x}_n is a four-dimensional vector of $(r, \theta_{\text{AZ}}, \theta_{\text{EL}}, D)$. After coordinates transformation to the Cartesian coordinate, \mathbf{x}_n goes to be (x, y, z, D) . We view the points in \mathbf{X} are independently drawn from the likelihood $p(\mathbf{X}|\mathbf{z})$, given a latent motion state \mathbf{z} which is a D -dimensional continuous vector. According to the Assumption 1, $p(\mathbf{X}|\mathbf{z})$ follows multivariate Gaussian distribution. The Bayes' theorem shows

$$p(\mathbf{z}|\mathbf{X}) = \frac{\underbrace{p(\mathbf{X}|\mathbf{z}) p(\mathbf{z})}_{\text{posterior}}}{\underbrace{p(\mathbf{X})}_{\text{evidence}}} = \frac{p(\mathbf{X}|\mathbf{z}) p(\mathbf{z})}{\int p(\mathbf{X}|\mathbf{z}) p(\mathbf{z}) d\mathbf{z}}. \quad (1)$$

We expect to infer the motion state \mathbf{z} based on the observation \mathbf{X} . This is equivalent to infer the posterior $p(\mathbf{z}|\mathbf{X})$ of \mathbf{z} . Due to the difficulties in solving $p(\mathbf{z}|\mathbf{X})$ analytically as the evidence $p(\mathbf{X})$ is usually intractable, two major approximation approaches, i.e Markov chain Monte Carlo (MCMC) and variational inference (VI), are mostly used.

Generally, the MCMC approach [30] uses sampling method to draw enough samples from a tractable proposal distribution which is eventually approximate to the target distribution $p(\mathbf{z}|\mathbf{X})$. The most commonly used MCMC algorithm iteratively samples a data \mathbf{z}^t from an arbitrary tractable proposal distribution $q(\mathbf{z}^t|\mathbf{z}^{(t-1)})$ at step t , and then accept it with a probability of

$$\begin{aligned} & \min\left\{1, \frac{p(\mathbf{z}^t|\mathbf{X}) * q(\mathbf{z}^t|\mathbf{z}^{(t-1)})}{p(\mathbf{z}^{(t-1)}|\mathbf{X}) * q(\mathbf{z}^{(t-1)}|\mathbf{z}^t)}\right\} \\ &= \min\left\{1, \frac{p(\mathbf{X}|\mathbf{z}^t) p(\mathbf{z}^t) * q(\mathbf{z}^t|\mathbf{z}^{(t-1)})}{p(\mathbf{X}|\mathbf{z}^{(t-1)}) p(\mathbf{z}^{(t-1)}) * q(\mathbf{z}^{(t-1)}|\mathbf{z}^t)}\right\}, \quad (2) \end{aligned}$$

where the difficult calculation of $p(\mathbf{X})$ has been circumvented. And it has been proven that this approach constructs a Markov chain whose equilibrium distribution equals to $p(\mathbf{z}|\mathbf{X})$ and is independent to the initial choice of $q(\mathbf{z}^0)$. One of the disadvantages in the MCMC approach is that the chain needs a long and indeterminable burn-in period to approximately reach the equilibrium distribution. This causes the MCMC not suitable for learning on large-scale dataset.

On the other hand, the VI approach [31] uses a family of tractable probability distribution $Q\{q(\mathbf{z})\}$ to approximate the true $p(\mathbf{z}|\mathbf{X})$ instead of solving it analytically. The VI approach changes the inference problem to a optimization problem as

$$q^*(\mathbf{z}) = \arg \min_{q(\mathbf{z}) \in Q} \text{KLD}\{q(\mathbf{z})||p(\mathbf{z}|\mathbf{X})\}, \quad (3)$$

where KLD is the KullbackLeibler divergence that measures the distance between two probability distributions. And by definition we have

$$\begin{aligned} & \text{KLD}\{q(\mathbf{z})||p(\mathbf{z}|\mathbf{X})\} \\ &:= \int q(\mathbf{z}) \log \frac{q(\mathbf{z})}{p(\mathbf{z}|\mathbf{X})} d\mathbf{z} \end{aligned}$$

$$\begin{aligned} &= \int q(\mathbf{z}) \log q(\mathbf{z}) d\mathbf{z} - \int q(\mathbf{z}) \log p(\mathbf{z}|\mathbf{X}) d\mathbf{z} \\ &= \mathbb{E}_q[\log q(\mathbf{z})] - \mathbb{E}_q[\log p(\mathbf{z}|\mathbf{X})] \\ &= \mathbb{E}_q[\log q(\mathbf{z})] - \mathbb{E}_q[\log p(\mathbf{X}|\mathbf{z})p(\mathbf{z})] + \mathbb{E}_q[\log p(\mathbf{X})] \\ &= \underbrace{\mathbb{E}_q[\log q(\mathbf{z})] - \mathbb{E}_q[\log p(\mathbf{X}|\mathbf{z})p(\mathbf{z})]}_{\mathcal{L}(q)} + \log p(\mathbf{X}), \quad (4) \end{aligned}$$

where $\mathbb{E}_q[*]$ is the statistical expectation operator of function $*$ whose variable follows $q(\mathbf{z})$, and \mathcal{L} is called the evidence low bound (ELBO). As the term $\log p(\mathbf{X})$ is constant with respect to \mathbf{z} , the optimization in Equ. (3) is simplified to be

$$q^*(\mathbf{z}) = \arg \min_{q(\mathbf{z}) \in Q} \mathcal{L}(q). \quad (5)$$

Here, the difficult computation of $p(\mathbf{X})$ is also circumvented. This optimization approach leads to one of the advantages of VI, that it can be integrated into a neural network framework and optimized through the back-propagation algorithm.

It is critical to choose the variational distribution $Q\{q(\mathbf{z})\}$ such that it is not only flexible enough to closely approximate the $p(\mathbf{z}|\mathbf{X})$, but also simple enough for efficient optimization. The most commonly used option is the factorized Gaussian family

$$q(\mathbf{z}) = \prod_{d=1}^D q(\mathbf{z}[d]) = \prod_{d=1}^D \mathcal{N}(\mathbf{z}[d]|\boldsymbol{\mu}_q[d], \boldsymbol{\sigma}_q[d]), \quad (6)$$

where $(\boldsymbol{\mu}_q, \boldsymbol{\sigma}_q)$ are mean and covariance of the distribution of latent variable \mathbf{z} with a predetermined length of D , and the components in \mathbf{z} are mutually independent.

D. Variational Autoencoder

As we briefly state previously, we adopt the semi-supervised anomaly detection approach to train model only on normal ADL such that the model will be surprised by the ‘unseen’ fall data. The common approach is autoencoder, whose basic architecture is shown in Fig. 3 (a). The autoencoder consists of two parts, i.e. encoder and decoder. In most cases, the decoder is simply a mirror of the encoder. The encoder compresses the input data \mathbf{X} to a latent feature vector \mathbf{z} with less dimensions, and reversely the decoder reconstructs \mathbf{X}' to be as close to \mathbf{X} as possible, based on the latent feature vector \mathbf{z} . Generally, the multilayer perceptrons (MLP) are used to model the non-linear mapping function between \mathbf{X} and \mathbf{z} , as the MLP is a powerful universal function approximator [32]. Beside a predetermined non-linear activation function, such as sigmoid/tanh, the MLP are characterized by its weights and biases. The training objective is to minimize the loss function between \mathbf{X} and \mathbf{X}' with respect to the weights and biases of encoder MLP and decoder MLP. The loss function could be cross-entropy for categorical classification problem or mean square error (MSE) for regression problem.

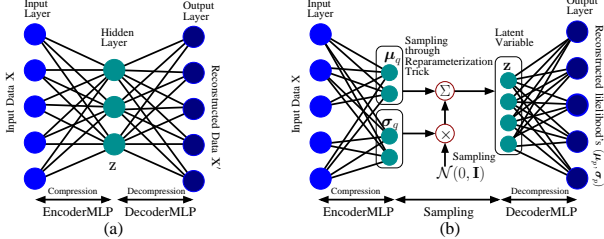


Fig. 3: Autoencoder architecture. (a) Vanilla autoencoder architecture. (b) Variational autoencoder architecture with factorized Gaussian parametrized by (μ_q, σ_q) .

In this way, the autoencoder squeezes the dimensionality to reduce the redundancy of input data. So it learns a compressed yet informative latent feature vector in \mathbf{X} . Therefore, the autoencoder will result in a close reconstruction \mathbf{X}' from the input data similar to \mathbf{X} , with a low reconstruction loss. However, whenever an ‘unseen’ data passes through, the autoencoder will erroneously squeeze it and be unable to reconstruct it well. This will lead a loss spike from which an anomaly can be detected.

Similarly, in the variational autoencoder (VAE) [33], [34] in Fig. 3 (b), the encoder learns $q(\mathbf{z})$ that aims to approximate $p(\mathbf{z}|\mathbf{X})$ from the input data \mathbf{X} using VI approach, and the decoder reconstructs the $p(\mathbf{X}|\mathbf{z})$ based on \mathbf{z} sampled from the learned $q(\mathbf{z})$. The training objective is as in Equ. 5. We can evaluate the loss function in VAE case further,

$$\begin{aligned} \mathcal{L}_{\text{VAE}} &= \mathbb{E}_q[\log q(\mathbf{z})] - \mathbb{E}_q[\log p(\mathbf{z})] - \mathbb{E}_q[\log p(\mathbf{X}|\mathbf{z})] \\ &= \text{KLD}\{q(\mathbf{z})||p(\mathbf{z})\} - \mathbb{E}_q[\log p(\mathbf{X}|\mathbf{z})]. \end{aligned} \quad (7)$$

For the variational distribution $q(\mathbf{z})$, the factorized Gaussian in Equ. 6 is used, and for the prior $p(\mathbf{z})$, a common choice of Gaussian $\mathcal{N}(\mathbf{z}|\mathbf{0}, \mathbf{I})$ is used as we do not have a strong assumption on it. Therefore, the first term in \mathcal{L}_{VAE} in Equ. (7) is reduced to

$$\begin{aligned} &\text{KLD}\{q(\mathbf{z})||p(\mathbf{z})\} \\ &= -\frac{1}{2} \sum_{d=1}^D \{1 + \log \sigma_q[d]^2 - \mu_q[d]^2 - \sigma_q[d]^2\}, \end{aligned} \quad (8)$$

where (μ_q, σ_q) is the mean and variance of the factorized Gaussian $q(\mathbf{z})$ with D -dimensional latent vector \mathbf{z} . See Appendix A for detailed derivation.

For the second term in \mathcal{L}_{VAE} in Equ. (7), it is reduced to

$$\begin{aligned} &\mathbb{E}_q[\log p(\mathbf{X}|\mathbf{z})] \\ &= \int q(\mathbf{z}) \log p(\mathbf{X}|\mathbf{z}) d\mathbf{z} \\ &\approx \log p(\mathbf{X}|\mathbf{z}) \\ &= \log \mathcal{N}(\mathbf{X}|\mu_p, \sigma_p) \\ &= \log \prod_{n=1}^N \mathcal{N}(\mathbf{x}_n|\mu_p, \sigma_p) \\ &= \sum_{n=1}^N \sum_{k=1}^K \log \mathcal{N}(\mathbf{x}_n[k]|\mu_p[k], \sigma_p[k]) \end{aligned}$$

$$\approx -\frac{1}{2} \sum_{n=1}^N \sum_{k=1}^K \left\{ \frac{(\mathbf{x}_n[k] - \mu_p[k])^2}{\sigma_p[k]^2} + \log \sigma_p[k]^2 \right\}, \quad (9)$$

where the third line is single-data Monte Carlo estimation, the single-data \mathbf{z} is sampled from $q(\mathbf{z})$; the fourth line comes from the Assumption 1 on the likelihood parametrized by (μ_p, σ_p) ; $\mathbf{X}=\{\mathbf{x}_n\}_{n=1}^N$ is the input point cloud, each point \mathbf{x}_n is a K -dimensional vector; $\log \sqrt{2\pi}$ in the last line is ignored as it is a constant.

From the first line to the second line in Equ. (9), a single sample of \mathbf{z} is needed. Instead of drawing from $q(\mathbf{z})$ directly, the reparameterization trick [33], [35] as following is used.

$$\mathbf{z} = \mu_p + \sigma_p \odot \epsilon, \quad (10)$$

where $\epsilon \sim \mathcal{N}(\mathbf{0}, \mathbf{I})$, \odot means element-wise production. And the trick is to draw a K -dimensional sample ϵ from $\mathcal{N}(\mathbf{0}, \mathbf{I})$, and then get \mathbf{z} through Equ. (10).

By viewing Equ. (8), the VAE encoder becomes clear as

$$(\mu_q, \log \sigma_q^2) = \text{EncoderMLP}_\phi\{\mathbf{X}\}, \quad (11)$$

where the weights and biases of encoder MLP are denoted as ϕ . In other words, the EncoderMLP_ϕ estimates the parameters of $q(\mathbf{z})$ from the input \mathbf{X} .

Similarly, by viewing Equ. (9), the VAE decoder becomes clear as

$$(\mu_p, \log \sigma_p^2) = \text{DecoderMLP}_\theta\{\mathbf{z}\}, \quad (12)$$

where the weights and biases of decoder MLP are denoted as θ . In other words, the DecoderMLP_θ estimates the parameters of $p(\mathbf{X}|\mathbf{z})$ from the \mathbf{z} sample got from Equ. (10).

Then the VAE architecture shown in Fig. 3 (b) becomes clear by combining EncoderMLP_ϕ and DecoderMLP_θ together, where these two parts are bridged through the sampling of \mathbf{z} . And the VAE training objective is to minimize the loss function, that is the subtraction of Equ. (8) from Equ. (9) according to Equ. (7), with respect to (ϕ, θ) .

E. Recurrent Autoencoder

While we use the VI approach to learn the radar point cloud distribution at each frame, we also need a sequence-to-sequence modeling approach to learn distribution changes over multiple frames as we stated in Section II-B previously.

The recurrent neural network (RNN) is such a basic sequence-to-sequence model for temporal applications. At every frame l , an RNN accepts two inputs, input from the sequence at the l -th frame x_l and its previous hidden state h_{l-1} , to output a new hidden state h_l , calculated as:

$$h_l = \tanh(W * h_{l-1} + U * x_l) \quad \forall l = 1, 2, \dots, L \quad (13)$$

where W and U are learnable weights (including the bias term, omitted for brevity), and L is the length of the sequence. Note that at $l=1$, h_0 is defined as the initial RNN state that is either initialized as zeros, or randomly initialized. Also note that the hidden state h_l acts as an accumulated memory state as it continuously computed and updated with new information in the sequence. However, in

[36], the primary shortcoming in RNNs in modeling long term dependencies, due to vanishing/exploding gradients, was thoroughly explored and identified. Long-Short-Term-Memory (LSTM) and Gated-Recurrent-Units (GRUs) were developed as a result, to overcome this challenge [37], [38].

In our case, as a fall motion may last for about one second, that is ten frames for the radar data rate of ten frames per second, the long term dependency is not an issue here. Only the basic RNN is used for light computation load consideration.

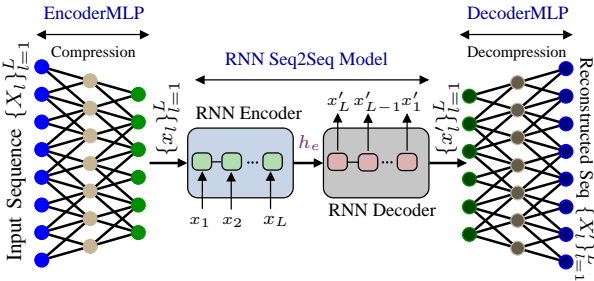


Fig. 4: A depiction of a Recurrent Autoencoder (RAE). The input sequence $\{\mathbf{X}_l\}_{l=1}^L$ is first compressed to a embedded feature sequence $\{x_l\}_{l=1}^L$ on per frame basis through the EncoderMLP. An RNN Encoder iteratively processes the data over L frames and the final hidden state h_e is passed on to the RNN Decoder that outputs the reconstructed embedded feature sequence $\{x'_l\}_{l=1}^L$ in reverse. Finally, $\{x'_l\}_{l=1}^L$ are decompressed to reconstruct the sequence $\{\mathbf{X}'_l\}_{l=1}^L$ through the DecoderMLP. The output sequence $\{\mathbf{X}'_l\}_{l=1}^L$ is compared with the input sequence $\{\mathbf{X}_l\}_{l=1}^L$ to compute the reconstruction loss, which is desired to be low for an autoencoder.

The RNN-based autoencoder [39] [40], or RAE shown in Fig. 4, is built upon the vanilla autoencoder architecture in Fig. 3 (a). As the input of RAE is a time sequence of feature vector, it has two dimensions, i.e. feature dimension and time dimension. Therefore, the RAE consists of two autoencoder substructures, responsible for each dimension respectively. In Fig. 4, the EncoderMLP/DecoderMLP is for compressing and reconstructing the feature vector on per frame basis, and the RNN-Encoder/Decoder is for compressing and reconstructing the time sequence over multiple frames. Overall, the RAE reduces redundancy in both feature and time dimension.

III. PROPOSED SYSTEM

To effectively learn the motion pattern of human body, which is formed by a sequence of radar point cloud data, for fall detection in a semi-supervised approach, we propose the Variational Recurrent Autoencoder (VRAE) which has two autoencoder substructures, i.e. VAE for learning radar point cloud distribution on per frame basis and RAE for learning the sequence over multiple frames. The VRAE is trained only on normal ADL, such that an ‘unseen’ fall will cause a spike in the loss, also called anomaly level. If the height of body centroid, which is estimated by mmWave radar sensor in parallel, drops suddenly at the same time, we claim a fall detection. The proposed system, called *mmFall*, including both hardware and software, is presented in Fig. 5.

A. Data Preprocessing

With a proper mmWave radar sensor, we are able to collect the radar point cloud as shown in Fig. 1 (b). In Fig. 5, the radar sensor could be mounted on the wall in a room with a height of h over the head of people, and could also be rotated with a angle θ_{tilt} so that it has a better coverage of the room. The radar sensor can detect multiple moving persons simultaneously, each person has an unique target ID as a result of the clustering/tracking algorithms. With the multiple frame data with the same target ID, we can analyze the motion of the person associated this target ID. In other words, each person’s motion analysis can be processed separately based on the target ID. Afterwards, we will only discuss single-person scenario for brevity.

We then propose a data preprocessing flow denoted in Fig. 5 for the following reasons.

The original measurement for each point in the radar point cloud is in the radar polar coordinates. We need to transfer it to the radar Cartesian coordinates, and then to the ground Cartesian coordinates on the basis of the tilt angle and height. Therefore, we have a transformation matrix as

$$\begin{bmatrix} x \\ y \\ z \end{bmatrix} = \begin{bmatrix} 1 & 0 & 0 \\ 0 & \cos \theta_{\text{tilt}} & -\sin \theta_{\text{tilt}} \\ 0 & \sin \theta_{\text{tilt}} & \cos \theta_{\text{tilt}} \end{bmatrix} \begin{bmatrix} r \cos \theta_{\text{EL}} \sin \theta_{\text{AZ}} \\ r \cos \theta_{\text{EL}} \cos \theta_{\text{AZ}} \\ r \sin \theta_{\text{EL}} \end{bmatrix} + \begin{bmatrix} 0 \\ 0 \\ h \end{bmatrix}, \quad (14)$$

where $(r, \theta_{\text{AZ}}, \theta_{\text{EL}})$ is range, azimuth angle and elevation angle in the radar polar coordinates, θ_{tilt} is radar tilt angle, h is the radar platform height, and $[x, y, z]^T$ is the result in the ground Cartesian coordinates.

After coordinate transformation, at each frame we obtain a radar point cloud, in which each point is a vector of (x, y, z, D) where D is the Doppler from the radar original measurement. And we also have the centroid (x_c, y_c, z_c) as a result of the clustering/tracking algorithms in the radar.

We accumulate the current frame’s previous L frames including itself as a motion pattern. The value of L equals to the radar frame rate in frames per second (fps) multiplied by the predetermined detection window in seconds. For each motion pattern with L frames, we subtract the x and y value of each point in each frame from the x_c and y_c value of centroid in the first frame, respectively. In this way, we shift the motion pattern to the origin of a reference coordinates.

Algorithm 1: Data Oversampling Method

Input: Input dataset $\mathbf{X} = \{\mathbf{x}_i\}_{i=1}^M$ with length of M , M is a random number, each data sample \mathbf{x}_i is a vector. N , target length after oversampling. N is always $\geq M$.

Output: $\mathbf{X}' = \{\mathbf{x}'_i\}_{i=1}^N$ with length of N .

```

1  $\hat{\mu} = \frac{1}{M} \sum_{i=1}^M \mathbf{x}_i$  // Get the estimated mean
2 for  $i = 1$  to  $N$  do
3   if  $i \leq M$  then // Rescale and shift
4      $\mathbf{x}'_i = \sqrt{\frac{N}{M}} \mathbf{x}_i + \hat{\mu} - \sqrt{\frac{N}{M}} \hat{\mu}$ ;
5   else // Pad with  $\hat{\mu}$ 
6      $\mathbf{x}'_i = \hat{\mu}$ ;
7   end
8 end

```

At each frame, the number of points is a random number due to the nature of radar measurement. To meet the fixed number of input nodes of VRAE model, we need

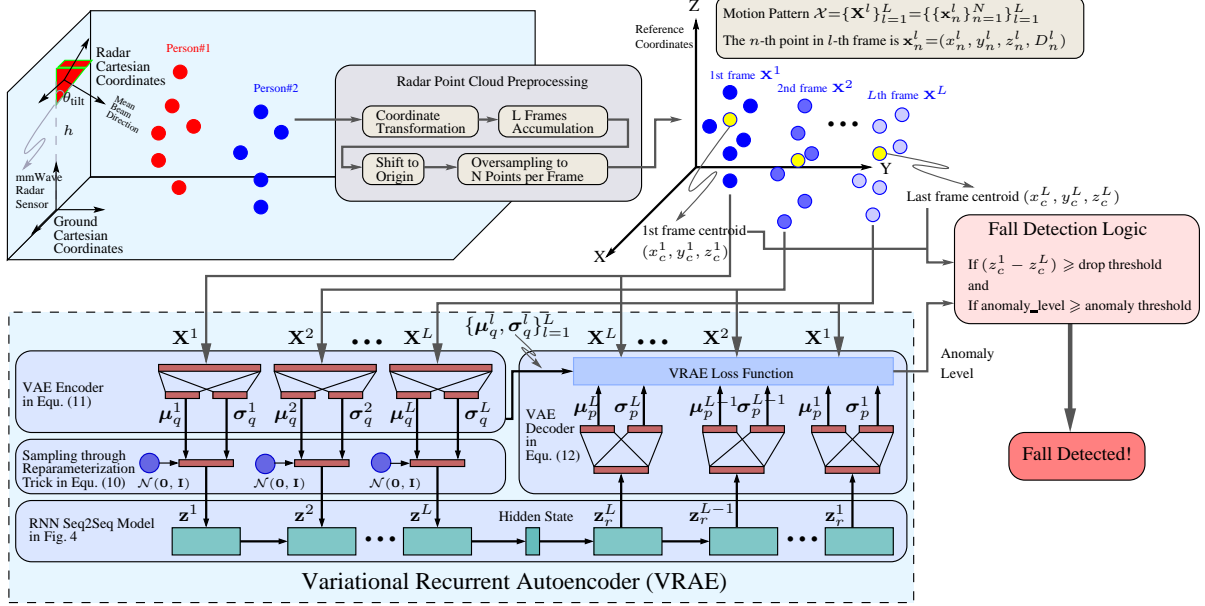


Fig. 5: An overview of the proposed *mmFall* System. At each frame, we obtain the point cloud of a human body along with its centroid from mmWave radar sensor. After the preprocessing stage, we get a motion pattern $\mathcal{X} = \{\mathbf{X}^l\}_{l=1}^L$ in the reference coordinates. For each l -th frame, we use the VAE Encoder to model the mean μ_q^l and variance σ_q^l of the factorized Gaussian family $q(\mathbf{z}^l) = \prod_{j=1}^D \mathcal{N}(z_j^l | \mu_j^l, \sigma_j^l)$ that aims to approximate the true posterior $p(\mathbf{z}^l | \mathbf{X}^l)$ of the latent motion state \mathbf{z}^l , where D is the predetermined length of \mathbf{z} . Then we use the reparameterization trick to sample \mathbf{z}^l from $q(\mathbf{z}^l)$. After we have a sequence of latent motion states $\mathcal{Z} = \{\mathbf{z}^1, \dots, \mathbf{z}^L\}$, we use the RAE to compress and then reconstruct it as $\mathcal{Z}_r = \{\mathbf{z}_r^1, \dots, \mathbf{z}_r^L\}$. Based on \mathcal{Z}_r , we use the VAE Decoder to model the mean μ_p^l and variance σ_p^l of the likelihood $p(\mathbf{X}^l | \mathbf{z}^l)$. With (μ_q, σ_q) , (μ_p, σ_p) and \mathcal{X} , we are able to compute the VRAE loss defined in Equ. 16 as an indication of anomaly level. In the fall detection logic, if a sudden drop of centroid height is detected at the same time when the VRAE outputs a anomaly spike, we claim a fall detection.

a data oversampling method. The traditional oversampling method in deep learning approach is such as zero-padding or random-padding. However, these methods disrupt the distribution of original input and are not suitable in this case as our purpose is to learn the distribution of radar point cloud. Therefore, we propose a novel data oversampling Algorithm 1 that extends the original point cloud to a fixed number while keeping its mean and covariance the same. The proof of this algorithm is in Appendix B.

Finally, we obtain a motion pattern \mathcal{X} in the reference coordinates,

$$\begin{aligned} \mathcal{X} = \{\mathbf{X}^l\}_{l=1}^L &= \{\{\mathbf{x}_n^l\}_{n=1}^N\}_{l=1}^L \\ &= \{\{(x_n^l, y_n^l, z_n^l, D_n^l)\}_{n=1}^N\}_{l=1}^L, \end{aligned} \quad (15)$$

where L is the number of frames in the motion pattern; N is the number of points at each frame; \mathbf{X}^l is l -th frame; \mathbf{x}_n^l is the n -th point in l -th frame, that is also a 4D vector of $(x_n^l, y_n^l, z_n^l, D_n^l)$. We also have the centroid $\{(x_c^l, y_c^l, z_c^l)\}_{l=1}^L$ over L frames. Afterwards, we use the superscript l to denote the frame index.

B. VRAE Model

We propose the variational recurrent autoencoder (VRAE) architecture as shown in Fig. 5 and detailed in the caption. The VRAE model is a combination of VAE and RAE, discussed in the previous section. The VRAE loss $\mathcal{L}_{\text{VRAE}}$

is the VAE loss \mathcal{L}_{VAE} in Equ. (7) over all the L frames. With substitution of Equ. (8) and (9), we have

$$\begin{aligned} \mathcal{L}_{\text{VRAE}} &= \sum_{l=1}^L \left\{ \text{KLD}\{q(\mathbf{z}^l) || p(\mathbf{z}^l)\} - \mathbb{E}_q[\log p(\mathbf{X}^l | \mathbf{z}^l)] \right\} \\ &= \sum_{l=1}^L \left\{ \frac{1}{2} \sum_{n=1}^N \sum_{k=1}^K \left\{ \frac{(\mathbf{x}_n^l[k] - \mu_p^l[k])^2}{\sigma_p^l[k]^2} + \log \sigma_p^l[k]^2 \right\} \right. \\ &\quad \left. - \frac{1}{2} \sum_{d=1}^D \{1 + \log \sigma_q^l[d]^2 - \mu_q^l[d]^2 - \sigma_q^l[d]^2\} \right\} \quad (16) \end{aligned}$$

where L , N and \mathbf{x}_n^l are from the motion pattern in Equ. (15); K is the length of point vector, in our case $K=4$ as each point is a 4D vector; D is the length of latent motion state \mathbf{z} ; (μ_q, σ_q) and (μ_p, σ_p) are parameters of factorized Gaussian $q(\mathbf{z})$ and likelihood $p(\mathbf{X} | \mathbf{z})$, respectively, both are modeled through the architecture in Fig. 5.

For VRAE training, the objective is to minimize $\mathcal{L}_{\text{VRAE}}$ with respect to the network parameters. The standard stochastic gradient descent algorithm Adam [34] is used.

It is noted that, for the implementation of VAE Encoder/Decoder in VRAE, only dense layer or fully-connected layer is used, as the model should be invariant to the order of point cloud at each frame.

C. Fall Detection Logic

In a semi-supervised learning approach, we train this VRAE model only on normal ADL, which are easily to collect compared to falls. For normal ADL, the VRAE will output a low $\mathcal{L}_{\text{VRAE}}$ as this is the training objective. In the inference stage, the model will generate a high loss $\mathcal{L}_{\text{VRAE}}$ when an ‘unseen’ motion happens, such as fall occurs. Therefore, we denote the VRAE loss $\mathcal{L}_{\text{VRAE}}$ as an anomaly level measure of human body motion.

Along with the body centroid height $\{z_c^l\}_{l=1}^L$ over L frames, we can calculate the drop of centroid height as $z_c^1 - z_c^L$ during this motion. Then we propose a fall detection logic as in Fig. 5, that is if the centroid height drop is greater than a threshold at the same time when the anomaly level is greater than a threshold, we claim a fall detection.

According to the World Health Organization (WHO) [2], fall is defined as “inadvertently coming to rest on the ground, floor or other lower level, excluding intentional change in position to rest in furniture, wall or other objects.” In the proposed *mmFall* system, the VRAE measures the inadvertence or anomaly level of the motion, while the centroid height drop indicates the motion of coming to rest on lower level.

IV. EXPERIMENTAL RESULTS AND DISCUSSION

To verify the effectiveness of proposed system, we used one mmWave radar sensor to collect experimental data and implemented the proposed *mmFall* system along with two other baselines, for performance evaluation and comparison.

A. Hardware Configuration and Experiment Setup

We adopt the Texas Instrument (TI) AWR1843BOOST mmWave FMCW radar evaluation board [41] for radar point cloud acquisition. This radar sensor has three transmitting antenna channels and four receiving antenna channels as shown in Fig. 1 (a). The middle transmitting channel is displaced above the other two by the distance of half a wavelength. Through the direction-of-angle (DOA) algorithm using multiple-input and multiple-output (MIMO), it can achieve 2x4 MIMO in azimuth and 2x1 MIMO in elevation. Thus, we have 3D positional measurement of each point. Plus the 1D Doppler, finally we have a 4D radar point cloud. Based on a demo project from TI, we configure the radar sensor with the parameters listed in Table I.

Based on the Robotic Operating System (ROS) on an Ubuntu laptop, we developed a interface program to connect the TI AWR1843BOOST and collect the radar point cloud data over the USB port. Then we set up the equipment in the living room (2.7m*8.2m*2.7m) in an apartment, as shown in Fig. 1 (a). The radar sensor was put on top of a tripod with height of 2 meters, and rotated with a tilt angle of 10 degrees for better area coverage.

TABLE I: mmWave FMCW radar parameter configuration. Refer to [42] for waveform details. f_s , FMCW starting frequency. BW, FMCW bandwidth. r_{Chirp} , FMCW chirp rate. f_{ADC} , ADC sampling rate. N_{Fast} , ADC samples per chirp. CPI, coherent processing interval. N_{Slow} , chirps per CPI per transmitting channel. T_{Frame} , duration of one frame. ΔR , range resolution. R_{max} , maximum unambiguous range. ΔD , Doppler resolution. D_{max} , maximum unambiguous Doppler. $\Delta\theta_{\text{AZ}}$, azimuth angle resolution. $\Delta\theta_{\text{EL}}$, elevation angle resolution. r_{Frame} , frame rate in frames per second.

Parameter	Value	Unit	Parameter	Value	Unit
f_s	77	GHz	ΔR	0.078	m
BW	1.92	GHz	R_{max}	9.99	m
r_{Chirp}	30	MHz/us	ΔD	0.079	m/s
f_{ADC}	2	MHz	D_{max}	± 2.542	m/s
N_{Fast}	128		MIMO	2x4/2x1	AZ/EL
CPI	24.2	ms	$\Delta\theta_{\text{AZ}}$	15	deg
N_{Slow}	64		$\Delta\theta_{\text{EL}}$	57	deg
T_{Frame}	100	ms	r_{Frame}	10	fps

B. Data Collection

During the experiment, we collected three dataset as in Table II. Firstly, we collected the D_0 dataset which contains about two hours of normal ADL without any labels, and it is for training purpose. Secondly, in the D_1 dataset, we collected randomly walking along with one sample of every other motions including fall, etc. We showed the motion pattern for every motion in Fig. 6 for visualization purpose. Lastly, we collected a comprehensive inference dataset D_2 and manually labeled the frame index when a fall happens as the ground truth, and it is used for overall performance evaluation. It is noted that in D_1 and D_2 , both the fall and jumping are anomaly that can not be found in D_0 . We expect that VRAE will output anomaly level spike for both fall and jumping, but the fall detection logic also involving the centroid height drop will guarantee the correct fall detection.

TABLE II: Collected Dataset.

Name	Description
D_0	Two hours of normal ADL, including randomly walking, sitting on the floor, crouching, bending, etc. No labeling.
D_1	Randomly walking with one forward fall, one backward fall, one left fall, one right fall, one sitting on the floor, one crouching, one bending, and one jumping.
D_2	Randomly walking with 15 forward falls, 15 backward falls, 10 left falls, 10 right falls, 50 sitting on the floor, 50 crouching, 50 bending, and 50 jumping. Labeling fall as ground truth.

C. Model Implementation and Two Baselines

Based on Tensorflow and Keras, we first implemented the proposed *mmFall* system in Fig. 5 with loss function in Equ. (16). In this implementation, we set the number of frames, L , equal to 10 for 1 second detection window with 10 fps radar data rate; the number of point each frame N equal to 64 for data oversampling. Thus, the motion pattern \mathcal{X} , i.e. the model input, is $10 \times 64 \times 4$. We set the length of latent motion state z , D , equal to 16. For performance comparison purpose, we also implemented two other baselines. All the three models are listed in Table III.

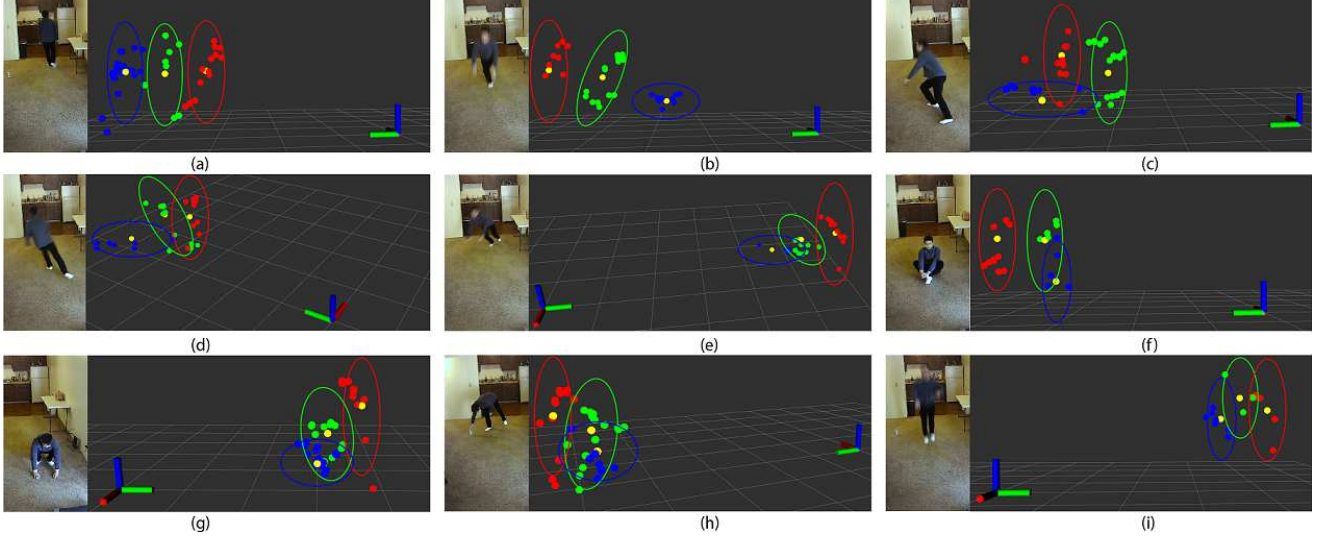


Fig. 6: Motion patterns in dataset D_1 along with the associated camera view. Only the ellipse was manually added for depicting the distribution of point cloud. For the points, different color indicates the frame in time order: red, green, and then blue, while the yellow point indicates the centroid estimated by the mmWave radar sensor. For simplicity, we showed the frames with the increment of five frames. Each frame is 0.1 seconds. Please compare this figure with Fig. 2. For the coordinates, red is the cross-radar direction, green is the forward direction, and blue is the height direction. (a) Randomly walking; (b) Forward fall; (c) Backward fall; (d) Left fall; (e) Right Fall; (f) Sitting down on the floor; (g) Crouching; (h) Bending; (i) Jumping.

The baseline VRAE_{SL} is the same as the proposed *mmFall* system except for using a simplified loss function in Equ. (17). The simplified loss function Equ. (17) is based on a weak assumption on likelihood, that is $p(\mathbf{X}|\mathbf{z})$ follows a Gaussian with identity covariance, i.e. $\mathcal{N}(\boldsymbol{\mu}_p, \mathbf{I})$. This leads to that the $\boldsymbol{\sigma}_p$ term in Equ. (16) is ignored, or

$$\mathcal{L}_{\text{VRAE_SL}} = \sum_{l=1}^L \left\{ \frac{1}{2} \sum_{n=1}^N \sum_{k=1}^K \{(\mathbf{x}_n^l[k] - \boldsymbol{\mu}_p^l[k])^2\} - \frac{1}{2} \sum_{d=1}^D \{1 + \log \boldsymbol{\sigma}_q^l[d]^2 - \boldsymbol{\mu}_q^l[d]^2 - \boldsymbol{\sigma}_q^l[d]^2\} \right\}. \quad (17)$$

To compare our proposed system with the baseline VRAE_{SL}, we will verify our assumption that the variance change of the radar point cloud distribution of human body carries better representation of motion, as discussed in Section II-B.

Another baseline is RAE with MSE loss in Fig. 4, which is similar to the proposed system except for using the vanilla MLP in the feature dimension instead of VI approach at each frame. To compare our proposed system with this baseline, we will show that the VI approach for motion state inference based on the distribution of radar point cloud makes more sense than the vanilla feature compression in RAE.

TABLE III: Implemented Models.

Name	Description
VRAE	The proposed variational recurrent autoencoder and fall detection logic in Fig. 5 with loss function in Equ. (16).
VRAE _{SL}	The proposed variational recurrent autoencoder and fall detection logic in Fig. 5 with simplified loss in Equ. (17).
RAE	The vanilla recurrent autoencoder in Fig. 4 with MSE loss function, and fall detection logic in Fig. 5.

D. Training and Inference

First, we trained these three models on the normal dataset D_0 , and then tested on dataset D_1 in which there are some normal motions as in D_0 and two different ‘unseen’ motions, i.e. fall and jumping, that do not appear in D_0 . The anomaly level outputted by these three models on D_1 is shown in Fig. 7. The proposed VRAE model can generate significant anomaly level for fall and jumping while keeping low for normal motions. Along with the fall detection logic involving body centroid drop, the jumping can be ignored, and only fall will be detected. As comparison, the VRAE_{SL} model suffers great noise during normal motions that easily leads to false alarm, and the vanilla RAE model can not learn the anomaly level effectively.

Finally, we tested these three well-trained models on the dataset D_2 . In D_2 , there are 50 falls with manually labeled ‘ground truth fall frame index’ when a fall happens, along with many other different motions without labeling. The fall detection logic will detect the frame index when a fall happens. We allow a flexible detection, i.e. if the ‘detected fall frame index’ falls into the 1-second detection window centered at one ‘ground truth fall frame index’, we treat it as true positive. In this experiment, for the fall detection logic we fixed the threshold of centroid height drop as 0.6 meters. By varying the anomaly level threshold, we got the receiver operating characteristic (ROC) curves as shown in Fig. 8. From this result, we clearly see that our proposed approach outperformed the other two baselines. Specifically, at the expense of two alarms, our VRAE model can achieve 98% fall detection rate out of 50 falls, while the VRAE_{SL} can only achieve around 60% and the vanilla RAE can only achieve around 38%.

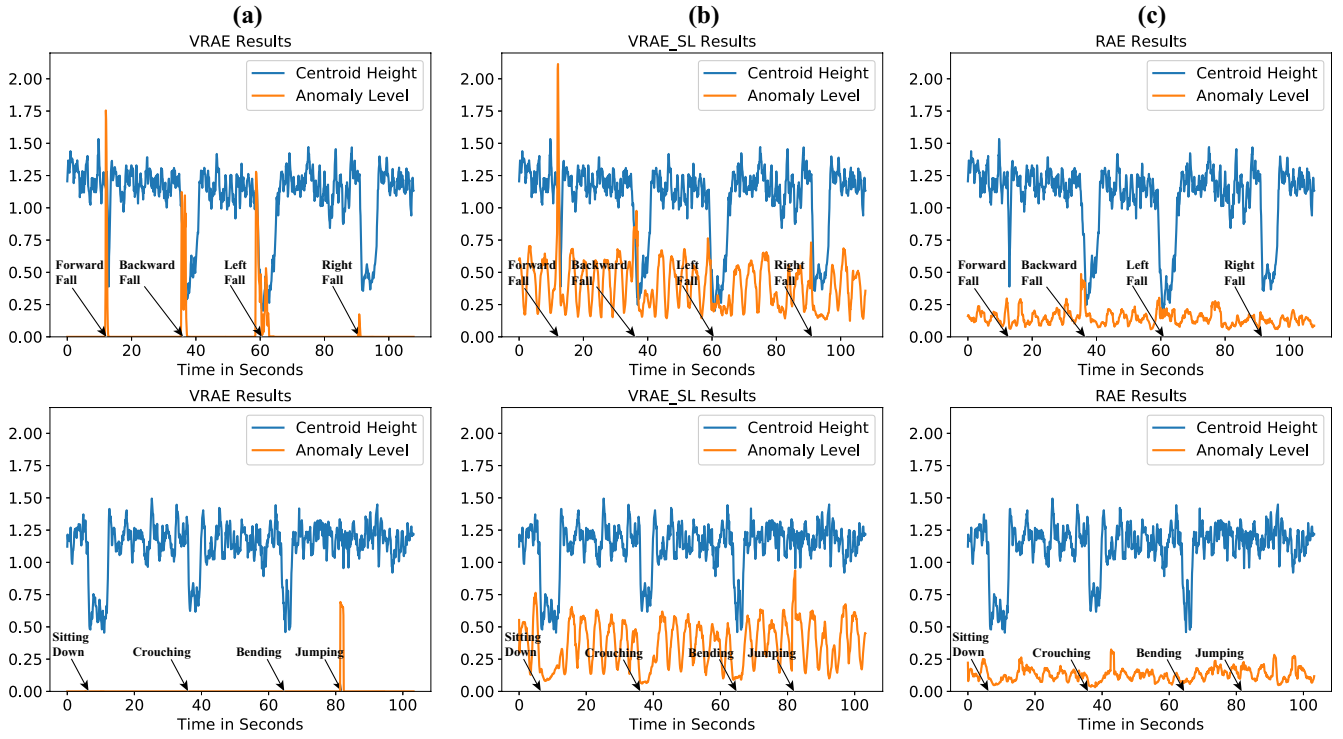


Fig. 7: Inference results of the models listed in Tab III on the dataset D_1 described in Tab II. In each figure, the blue lines represents the body's centroid height, and the orange line represents the model's loss output, or anomaly level. Only the black text and arrows were manually added as the ground truth when a motion happens. Except for the motion indicated by the black text, the rest of time are always randomly walking. (a) VRAE inference results: The VRAE model can clearly generate a spike in anomaly level when fall/jumping happens while keeping low anomaly level for normal motions. Jumping is another abnormal motion that does not appear in the training dataset D_0 , but the fall detection logic involving the body centroid drop at the same time will ignore jumping. On the other hand, without the help of anomaly level it is difficult to distinguish fall from other motions if only the change of centroid height is considered; (b) VRAE_SL inference results: The VRAE_SL can also have anomaly level spike generation for fall/jumping but suffer significant noise during normal motion occurrence. For example, the ‘Sitting Down’ and the ‘Right Fall’ have almost the same anomaly level output. As a result, either the ‘Sitting Down’ causes a false alarm, or ‘Right Fall’ causes a missed detection, depending on the threshold; (c) Vanilla RAE inference results: The vanilla RAE model can not effectively learn the anomaly level for ‘unseen’ motions.

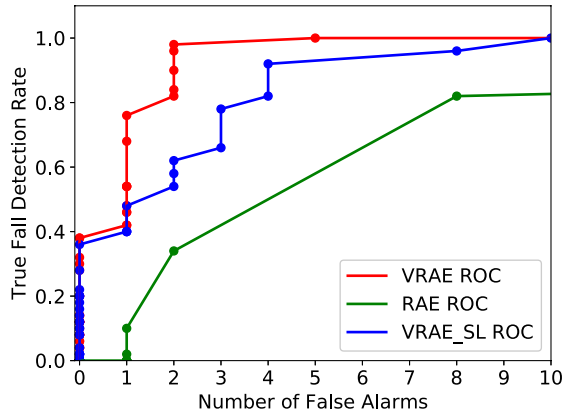


Fig. 8: ROC curves for all the three models.

V. CONCLUSION

In this study, we used a mmWave radar sensor for fall detection on the basis of its advantages such as privacy-compliant, non-wearable, sensitive to motions, etc. We made an assumption that the radar point cloud for human body can be viewed as a multivariate Gaussian distribution, and the distribution change over multiple frames has a unique

pattern for different motions. And then we proposed a variational recurrent autoencoder to effectively learn the anomaly level of ‘unseen’ motion, such as fall, that does not appear in the normal training dataset. We also involved a fall detection logic that checks the body centroid drop to further confirm the anomaly motion is fall. In this way, we detected the fall in an semi-supervised learning approach that does not require the difficult fall data collection and labeling. The experiment results showed our proposed system can achieve 98% detection rate out of 50 falls at the expense of just two false alarms, and outperformed the other two baselines.

APPENDIX A PROOF OF EQU. 8

$$\begin{aligned}
 & \text{KLD}\{q(\mathbf{z})||p(\mathbf{z})\} \\
 &= \text{KLD}\left\{\prod_{d=1}^D \mathcal{N}(\mathbf{z}[d]|\boldsymbol{\mu}_q[d], \boldsymbol{\sigma}_q[d])||\mathcal{N}(\mathbf{z}|\mathbf{0}, \mathbf{I})\right\} \\
 &:= \int \dots \int \prod_{d=1}^D \mathcal{N}(\mathbf{z}[d]|\boldsymbol{\mu}_q[d], \boldsymbol{\sigma}_q[d]) *
 \end{aligned}$$

$$\begin{aligned}
& \log \frac{\prod_{d=1}^D \mathcal{N}(\mathbf{z}[d] | \boldsymbol{\mu}_q[d], \boldsymbol{\sigma}_q[d])}{\prod_{d=1}^D \mathcal{N}(\mathbf{z}[d] | 0, 1)} d\mathbf{z}[1] \dots d\mathbf{z}[D] \\
&= \int \dots \int \prod_{d=1}^D \mathcal{N}(\mathbf{z}[d] | \boldsymbol{\mu}_q[d], \boldsymbol{\sigma}_q[d]) * \\
& \quad \sum_{d=1}^D \log \frac{\mathcal{N}(\mathbf{z}[d] | \boldsymbol{\mu}_q[d], \boldsymbol{\sigma}_q[d])}{\mathcal{N}(\mathbf{z}[d] | 0, 1)} d\mathbf{z}[1] \dots d\mathbf{z}[D] \\
&= \sum_{d=1}^D \int \mathcal{N}(\mathbf{z}[d] | \boldsymbol{\mu}_q[d], \boldsymbol{\sigma}_q[d]) \log \frac{\mathcal{N}(\mathbf{z}[d] | \boldsymbol{\mu}_q[d], \boldsymbol{\sigma}_q[d])}{\mathcal{N}(\mathbf{z}[d] | 0, 1)} d\mathbf{z}[d] \\
&= \sum_{d=1}^D \int \mathcal{N}(\mathbf{z}[d] | \boldsymbol{\mu}_q[d], \boldsymbol{\sigma}_q[d]) * \\
& \quad \{ \log \frac{1}{\boldsymbol{\sigma}_q[d]^2} - \frac{(\mathbf{z}[d] - \boldsymbol{\mu}_q[d])^2}{2\boldsymbol{\sigma}_q[d]^2} + \frac{\mathbf{z}[d]^2}{2} \} d\mathbf{z}[d] \\
&= -\frac{1}{2} \sum_{d=1}^D \{ 1 + \log \boldsymbol{\sigma}_q[d]^2 - \boldsymbol{\mu}_q[d]^2 - \boldsymbol{\sigma}_q[d]^2 \}, \quad (18)
\end{aligned}$$

where $(\boldsymbol{\mu}_q, \boldsymbol{\sigma}_q)$ is the mean and variance of the factorized Gaussian $q(\mathbf{z})$ with D -dimensional latent vector \mathbf{z} .

APPENDIX B PROOF OF PROPOSED ALGORITHM

Given a set of statistically independent and identically distributed (i.i.d.) data $\mathbf{X} = \{\mathbf{x}_i\}_{i=1}^M$ drawn from a multivariate Gaussian random variable $\mathcal{N}(\boldsymbol{\mu}, \boldsymbol{\sigma})$, thus the maximum likelihood (ML) estimator of its mean $\boldsymbol{\mu}$ and covariance $\boldsymbol{\sigma}$ is,

$$\begin{aligned}
\hat{\boldsymbol{\mu}} &= \frac{1}{M} \sum_{i=1}^M \mathbf{x}_i, \\
\hat{\boldsymbol{\sigma}} &= \frac{1}{M} \sum_{i=1}^M \{\mathbf{x}_i - \hat{\boldsymbol{\mu}}\}^2. \quad (19)
\end{aligned}$$

For the output dataset $\mathbf{X}' = \{\mathbf{x}'_i\}_{i=1}^N$, its first M elements are modified from the input dataset according to Step 4 in Algorithm (1), and its last $(N - M)$ elements are simply the mean of the input dataset according to Step 6 in Algorithm (1). Thus, its ML estimator of its mean $\boldsymbol{\mu}'$ and covariance $\boldsymbol{\sigma}'$ is

$$\begin{aligned}
\hat{\boldsymbol{\mu}}' &= \frac{1}{N} \sum_{i=1}^N \mathbf{x}'_i \\
&= \frac{1}{N} \left\{ \sum_{i=1}^M \left(\sqrt{\frac{N}{M}} \mathbf{x}_i + \hat{\boldsymbol{\mu}} - \sqrt{\frac{N}{M}} \hat{\boldsymbol{\mu}} \right) + \sum_{i=M+1}^N \hat{\boldsymbol{\mu}} \right\} \\
&= \frac{1}{N} \left\{ \sqrt{\frac{N}{M}} \sum_{i=1}^M \mathbf{x}_i + M\hat{\boldsymbol{\mu}} - M\sqrt{\frac{N}{M}} \hat{\boldsymbol{\mu}} + (N - M)\hat{\boldsymbol{\mu}} \right\} \\
&= \frac{1}{N} \left\{ \sqrt{\frac{N}{M}} M\hat{\boldsymbol{\mu}} + M\hat{\boldsymbol{\mu}} - M\sqrt{\frac{N}{M}} \hat{\boldsymbol{\mu}} + (N - M)\hat{\boldsymbol{\mu}} \right\} \\
&= \frac{1}{N} \{N\hat{\boldsymbol{\mu}}\} = \hat{\boldsymbol{\mu}}, \quad (20)
\end{aligned}$$

and

$$\begin{aligned}
\hat{\boldsymbol{\sigma}}' &= \frac{1}{N} \sum_{i=1}^N \{\mathbf{x}'_i - \hat{\boldsymbol{\mu}}'\}^2 = \frac{1}{N} \sum_{i=1}^N \{\mathbf{x}'_i - \hat{\boldsymbol{\mu}}\}^2 \\
&= \frac{1}{N} \sum_{i=1}^M \left\{ \sqrt{\frac{N}{M}} \mathbf{x}_i + \hat{\boldsymbol{\mu}} - \sqrt{\frac{N}{M}} \hat{\boldsymbol{\mu}} - \hat{\boldsymbol{\mu}} \right\}^2 + \frac{1}{N} \sum_{i=(M+1)}^N \{\hat{\boldsymbol{\mu}} - \hat{\boldsymbol{\mu}}\}^2 \\
&= \frac{1}{N} \sum_{i=1}^M \left\{ \sqrt{\frac{N}{M}} \mathbf{x}_i - \sqrt{\frac{N}{M}} \hat{\boldsymbol{\mu}} \right\}^2 \\
&= \frac{1}{M} \sum_{i=1}^M \{\mathbf{x}_i - \hat{\boldsymbol{\mu}}\}^2 = \hat{\boldsymbol{\sigma}}. \quad (21)
\end{aligned}$$

Therefore, the proposed algorithm oversamples the original input dataset to a fixed number while keeping the ML estimation of mean and variance the same.

REFERENCES

- [1] *World Population Prospects 2019: Highlights (ST/ESA/SER.A/423)*, Department of Economic and Social Affairs, Population Division, United Nations, 2019. [Online]. Available: https://population.un.org/wpp/Publications/Files/WPP2019_Highlights.pdf
- [2] *WHO Global Report on Falls Prevention in Older Age*, World Health Organization, 2008. [Online]. Available: <https://extranet.who.int/agefriendlyworld/wp-content/uploads/2014/06/WHO-Global-report-on-falls-prevention-in-older-age.pdf>
- [3] (2018, Jan.) Falls. World Health Organization. [Online]. Available: <https://www.who.int/news-room/fact-sheets/detail/falls>
- [4] E. R. Burns, J. A. Stevens, and R. Lee, "The direct costs of fatal and non-fatal falls among older adultsUnited States," *J. Safety Res.*, vol. 58, pp. 99–103, 2016.
- [5] F. Li *et al.*, "Exercise and fall prevention: narrowing the research-to-practice gap and enhancing integration of clinical and community practice," *J. Am. Geriatr. Soc.*, vol. 64, no. 2, pp. 425–431, 2016.
- [6] T. Tamura *et al.*, "A wearable airbag to prevent fall injuries," *IEEE Trans. Inf. Technol. Biomed.*, vol. 13, no. 6, pp. 910–914, Nov 2009.
- [7] P. Di *et al.*, "Fall detection and prevention control using walking-aid cane robot," *IEEE/ASME Trans. Mechatronics*, vol. 21, no. 2, pp. 625–637, April 2016.
- [8] K. Chacour *et al.*, "From fall detection to fall prevention: A generic classification of fall-related systems," *IEEE Sens. J.*, vol. 17, no. 3, pp. 812–822, Feb 2017.
- [9] J. K. Lee, S. N. Robinovitch, and E. J. Park, "Inertial sensing-based pre-impact detection of falls involving near-fall scenarios," *IEEE Trans. Neural Syst. Rehabil. Eng.*, vol. 23, no. 2, pp. 258–266, March 2015.
- [10] J. Liu and T. E. Lockhart, "Development and evaluation of a prior-to-impact fall event detection algorithm," *IEEE Trans. Biomed. Eng.*, vol. 61, no. 7, pp. 2135–2140, July 2014.
- [11] J. Sun *et al.*, "A plantar inclinometer based approach to fall detection in open environments," in *Emerging Trends and Advanced Technologies for Computational Intelligence*. Springer, 2016, pp. 1–13.
- [12] B. Mirmahboub *et al.*, "Automatic monocular system for human fall detection based on variations in silhouette area," *IEEE Trans. Biomed. Eng.*, vol. 60, no. 2, pp. 427–436, Feb 2013.
- [13] Y. Li, K. Ho, and M. Popescu, "A microphone array system for automatic fall detection," *IEEE Trans. Biomed. Eng.*, vol. 59, no. 5, pp. 1291–1301, 2012.
- [14] K. Chacour *et al.*, "Smart carpet using differential piezoresistive pressure sensors for elderly fall detection," in *Proc. IEEE 11th Int. Conf. Wireless and Mobile Computing, Networking and Communications (WiMob)*, 2015, pp. 225–229.
- [15] X. Fan *et al.*, "Robust unobtrusive fall detection using infrared array sensors," in *Proc. IEEE Int. Conf. Multisensor Fusion and Integration for Intelligent Systems (MFI)*, 2017, pp. 194–199.
- [16] Y. Wang, K. Wu, and L. M. Ni, "Wifall: Device-free fall detection by wireless networks," *IEEE Trans. Mobile Comput.*, vol. 16, no. 2, pp. 581–594, Feb 2017.

- [17] Z.-P. Bian *et al.*, “Fall detection based on body part tracking using a depth camera,” *IEEE J. Biomed. Health Informat.*, vol. 19, no. 2, pp. 430–439, 2014.
- [18] M. G. Amin *et al.*, “Radar signal processing for elderly fall detection: The future for in-home monitoring,” *IEEE Signal Process. Mag.*, vol. 33, no. 2, pp. 71–80, March 2016.
- [19] G. Koshmak, A. Loutfi, and M. Linden, “Challenges and issues in multisensor fusion approach for fall detection: Review paper,” *J. Sens.*, vol. 2016, no. 6931789, 2016.
- [20] *mmWave radar sensors in robotics applications*, Texas Instruments, 2017. [Online]. Available: <http://www.ti.com/lit/wp/spry311/spry311.pdf>
- [21] L. Ren and Y. Peng, “Research of fall detection and fall prevention technologies: A systematic review,” *IEEE Access*, vol. 7, pp. 77702–77722, 2019.
- [22] S. Z. Gurbuz and M. G. Amin, “Radar-based human-motion recognition with deep learning: Promising applications for indoor monitoring,” *IEEE Signal Process. Mag.*, vol. 36, no. 4, pp. 16–28, July 2019.
- [23] B. Y. Su *et al.*, “Doppler radar fall activity detection using the wavelet transform,” *IEEE Trans. Biomed. Eng.*, vol. 62, no. 3, pp. 865–875, 2014.
- [24] B. Jokanović and M. Amin, “Fall detection using deep learning in range-doppler radars,” *IEEE Trans. Aerosp. Electron. Syst.*, vol. 54, no. 1, pp. 180–189, 2017.
- [25] V. Chandola, A. Banerjee, and V. Kumar, “Anomaly detection: A survey,” *ACM Comput. Surv.*, vol. 41, no. 3, Jul. 2009.
- [26] *Operation of Radar Services in the 76-81 GHz Band*, Federal Communications Commission, Washington, D.C. [Online]. Available: <https://docs.fcc.gov/public/attachments/FCC-15-16A1.pdf>
- [27] *Google LLC Request for Waiver of Part 15 for Project Soli*, Federal Communications Commission, Washington, D.C. [Online]. Available: <https://docs.fcc.gov/public/attachments/DA-18-1308A1.pdf>
- [28] G. Hakobyan and B. Yang, “High-performance automotive radar: A review of signal processing algorithms and modulation schemes,” *IEEE Signal Process. Mag.*, vol. 36, no. 5, pp. 32–44, 2019.
- [29] S. Blackman, *Multiple-target Tracking with Radar Applications*, ser. Radar Library. Dedham, MA: Artech House, 1986, ch. 11.
- [30] C. M. Bishop, *Pattern recognition and machine learning*, ser. Information science and statistics. New York, NY: Springer, 2006, ch. 11.
- [31] D. M. Blei, A. Kucukelbir, and J. D. McAuliffe, “Variational inference: A review for statisticians,” *J. Am. Stat. Assoc.*, vol. 112, no. 518, pp. 859–877, 2017.
- [32] S. Haykin, *Neural Networks and Learning Machines*, 3rd ed. Upper Saddle River, NJ: Pearson Higher Ed, 2011, ch. 4.
- [33] D. P. Kingma and M. Welling, “Auto-encoding variational bayes,” in *Proc. Int. Conf. Learning Representations (ICLR)*, 2014.
- [34] D. P. Kingma and M. Welling, “An introduction to variational autoencoders,” *Foundations and Trends in Machine Learning*, vol. 12, no. 4, pp. 307–392, 2019.
- [35] D. J. Rezende, S. Mohamed, and D. Wierstra, “Stochastic backpropagation and approximate inference in deep generative models,” in *Proc. 31st Int. Conf. Machine Learning (ICML)*, 2014, pp. II–1278–II–1286.
- [36] Y. Bengio, P. Simard, and P. Frasconi, “Learning long-term dependencies with gradient descent is difficult,” *IEEE Trans. Neural Netw.*, vol. 5, no. 2, pp. 157–166, 1994.
- [37] S. Hochreiter and J. Schmidhuber, “Long short-term memory,” *Neural computation*, vol. 9, no. 8, pp. 1735–1780, 1997.
- [38] K. Cho *et al.*, “Learning phrase representations using RNN encoder-decoder for statistical machine translation,” in *Proc. Conf. Empirical Methods in Natural Language Processing (EMNLP)*, 2014, pp. 1724–1734.
- [39] A. M. Dai and Q. V. Le, “Semi-supervised sequence learning,” in *Advances in Neural Information Processing Systems (NIPS)*, 2015, pp. 3079–3087.
- [40] T. Kieu *et al.*, “Outlier detection for time series with recurrent autoencoder ensembles,” in *Proc. 28th Int. Joint Conf. Artificial Intelligence (IJCAI)*, 2019, pp. 2725–2732.
- [41] *xWR1843 Evaluation Module (xWR1843BOOST) Single-Chip mmWave Sensing Solution*, Texas Instruments, 2019. [Online]. Available: <http://www.ti.com/lit/ug/spruim4a/spruim4a.pdf>
- [42] *Programming Chirp Parameters in TI Radar Devices*, Texas Instruments, 2020. [Online]. Available: <http://www.ti.com/lit/an/swra553a/swra553a.pdf>